International Journal of Mechanical Sciences 262 (2024) 108753

Contents lists available at ScienceDirect

International Journal of Mechanical Sciences

journal homepage: www.elsevier.com/locate/ijmecsci

Crack tip dislocation activity in refractory high-entropy alloys

Shuai Chen [a,b], Zachary H. Aitken [b], Subrahmanyam Pattamatta [c], Zhaoxuan Wu [d], Zhi Gen Yu [b], David J. Srolovitz [c,*], Peter K. Liaw [e,*], Yong-Wei Zhang [b,*]

[a] *Materials Genome Institute, Shanghai University, Shanghai 200444, China*
[b] *Institute of High Performance Computing (IHPC), Agency for Science, Technology and Research (A*STAR), 1 Fusionopolis Way, #16-16 Connexis, Singapore 138632, Republic of Singapore*
[c] *Department of Mechanical Engineering, The University of Hong Kong, Hong Kong Special Administrative Region of China*
[d] *Department of Materials Science and Engineering, City University of Hong Kong, Hong Kong Special Administrative Region of China*
[e] *Department of Materials Science and Engineering, The University of Tennessee, Knoxville, TN 37996, USA*

ARTICLE INFO

Keywords:
Refractory high-entropy alloys
Short-range ordering
Dislocation nucleation
Dislocation breakup
Dislocation annihilation

ABSTRACT

Dislocation activities play an important role in the deformation and failure of refractory high-entropy alloys (RHEAs). However, the impact of chemical short-range ordering (SRO) on dislocation activities at a crack tip in RHEAs remains unclear. Here, we investigate the effect of SRO on the dislocation nucleation, propagation, and reaction at a crack tip in a body-centered-cubic (BCC) MoTaTiWZr RHEA, using a combination of molecular dynamic simulations and Monte Carlo methods. Our results indicate that this RHEA is energetically favorable to form SRO, developing a pseudo-composite microstructure with low-energy clusters (LECs), medium-energy clusters (MECs), and high-energy clusters (HECs). The HECs at the crack tip are favorable sites for dislocation nucleation whereas the MECs surrounding the HECs function as a strong matrix to stabilize the weak HECs. At elevated temperatures, the HECs near the crack tip transform to severely distorted BCC and disordered structures, which can cause the breakup, absorption, and annihilation of emitted dislocations and nucleation of new dislocations. Our work reveals the interesting role of SRO in altering the dislocation activities at the crack tip of RHEAs and suggests alternative routes for designing superior RHEAs at both room and elevated temperatures.

1. Introduction

Compositionally complex [1] or high-entropy alloys [2] (HEAs), which are composed of five (or more) metallic elements with equal (or near-equal) atomic concentrations, have attracted extensive attentions due to the enormous potential for finding and developing new alloys with exciting and valuable new properties [3–5]. Refractory HEAs (RHEAs), one prominent class of HEAs made of refractory elements (Mo, Nb, Ta, Ti, V, W, Zr, etc.) and in a body-centered-cubic (BCC) lattice, possess high yield strength [6,7], superior thermal stability [8], excellent irradiation resistance [9], remarkable creep resistance [10] and outstanding tribological properties [11,12], which are recognized as promising candidates for structural materials under harsh conditions.

Dislocation activities play an important role in the plastic deformation and failure of RHEAs [6,7,13]. There are several well-established approaches to examine the dislocations in HEAs, including the solute-strengthening theory based on the fundamental interaction energy between a dislocation and the solutes that constitute the random alloys [14–16]. For example, Maresca et al. [15] demonstrated that the solute-strengthening theory could quantitatively capture the strength versus temperature for both MoNbTaW and MoNbTaVW alloys. Using the solute-strengthening theory, Yin et al. [16] revealed the special role of V in strengthening both the face-centered-cubic (FCC) CoCrFeMnNiV and BCC CrMoNbTaVWHfTiZr HEAs, i.e., the atomic volume is large in the FCC alloys and small in the BCC alloys, thus leading to a large misfit volume in both crystalline structures.

Refractory HEAs normally exhibit outstanding strength at ultra-high temperatures, but suffer from room-temperature brittleness. Researchers strive to improve the ductility of RHEAs at room temperature. Utilized natural-mixing characteristics among refractory elements, Wei et al. [17] designed a $Ti_{38}V_{15}Nb_{23}Hf_{24}$ RHEA that exhibits >20 % tensile ductility in the as-cast state, and physicochemical stability at high temperatures. Wang et al. [18] successfully achieved large plasticity of >10 %, along with high strength of >1750 MPa in the NbMoTaW RHEAs via grain boundary engineering with the addition of either metalloid B or C. Recently, Gou et al. [19] fabricated a TiZrHfNb RHEA with a room

---

* Corresponding authors.
E-mail addresses: srol@hku.hk (D.J. Srolovitz), pliaw@utk.edu (P.K. Liaw), zhangyw@ihpc.a-star.edu.sg (Y.-W. Zhang).

https://doi.org/10.1016/j.ijmecsci.2023.108753
Received 19 April 2023; Received in revised form 29 August 2023; Accepted 11 September 2023

temperature tensile yield strength of ~1034 MPa and ductility of ~18.5 % by increasing Nb contents to stabilize the BCC phase and suppresses the ω phase formation. Li et al. [20] designed a $(W_{1.5}Ni_{2.25}Fe)_{95}Ta_5$ RHEA with a stepwise and independently controllable dual coherent precipitation structure to facilitate the dislocation transmission and relieve the stress concentrations, exhibiting an ultrahigh strength of 2.15 GPa with a tensile ductility of 15 % at ambient temperature.

In a pioneering work, Rice [21] proposed a simple criterion to differentiate the brittle versus ductile behavior of a material, that is, when the ratio between the surface energy (γ_{surf}) and unstable stacking fault energy (γ_{usf}) of the material is larger (smaller) than 1, the material should be ductile (brittle). Remarkably, Hu et al. [22] performed a systematic screening of γ_{surf} and γ_{usf} over 112,378 alloy compositions among Ti, Zr, Hf, V, Nb, Ta, Mo, V, Re, and Ru to search for alloy candidates that possess enhanced strength-ductility synergies. Their search results were further supported by additional first-principles calculations. However, the above solute-strengthening theory and Rice criterion assume the condition of an ideal random solid solution (RSS).

Recent experimental studies have evidently demonstrated the prevalence of short-range ordering (SRO) in HEAs (including RHEAs) [23–25] and medium-entropy alloys [26–28]. For example, Ding et al. [24] demonstrated pronounced SRO in FCC CoCrFeNiPd, and Chen et al. [27] revealed the strong SRO in VCoNi via transmission electron microscopy. Lee et al. [28] observed local chemical ordering in the single phase NbTaTiV, where Nb-/Ta-rich regions and Ti-/V-rich regions are formed during solidification. Therefore, to understand the effect of SRO on dislocation activities in RHEAs is of great significance to facilitate the rational design of RHEAs. It has been reported that the atomic-level SRO or segregation plays an important role in tuning the dislocation activities and phase transformations in Cantor-like FCC HEAs [24,29–31]. These observations raise several interesting and yet important questions for BCC RHEAs. Can SRO also tune the dislocation activities in BCC RHEAs? How does SRO affect the dislocation activities at a crack tip in BCC RHEAs? Is there any difference in the dislocation activities between room and elevated temperatures? Answering these interesting questions provides the motivation for this current study.

Since SRO is at the length scale of the atomic level, it is highly challenging to trace its formation and/or evolution in HEAs experimentally. Atomistic simulations are a powerful tool to reveal the fundamental mechanisms behind the atomic-level events in HEAs. Density-functional theory (DFT) calculations of RHEAs are limited to special quasi-random structures (SQS) [32] and a small set of ordered structures (SSOS) [33,34] methods due to the high computational cost. A cluster expansion model based on DFT has been proposed by Alvarado et al. [35] to predict the SRO and thermodynamic properties in chemically complex systems and apply it to the WTaCrVHf quinary alloy. The simulation results indicate that the addition of Hf significantly modifies the SRO, mainly at intermediate to low temperatures, matching their experimental observations.

Molecular dynamics (MD) simulations are capable of exploring mechanical behavior and deformation mechanism in MEAs and HEAs on a larger size scale [36–39]. For example, Xie et al. [37] performed MD simulations to investigate the shock-induced phase transition for CoCrCuFeNi HEAs in terms of the crystallographic direction and shock velocity. Gao et al. [38] examined the mechanical properties of CoCrCuFeNi HEAs with defects (voids) via MD and demonstrated that dislocation emission occurs initially from the surface of the void.

Combining with Monte Carlo (MC) method, MD simulations were also used to study the SRO in HEAs and MEAs [40–45]. For example, He et al. [41] employed hybrid MC and MD to explore the influence of elemental segregation at grain boundaries (GBs) on the mechanical properties of CoCrCuFeNi HEAs under uniaxial load. Their results indicated that the transition from strengthening to weakening is closely related to the GB segregated Cu concentration [41]. Li et al. [42] performed MC and MD to study the shock-induced deformation and spallation of CoCrFeNiMn HEAs. The results show that SRO can only slightly increase the shear stress and the spall strength, but it can cause a reduction of ductility during the spallation.

For RHEAs, Yin et al. [43] studied the mechanisms underlying the mobility of edge and screw dislocations in BCC MoNbTaW without cracking and found that the mobility of edge dislocations was enhanced by SRO. In contrast, the rate of the double-kink nucleation in the motion of screw dislocations was reduced by SRO [43], which can have a significant impact on the mechanical property of RHEAs. Wang et al. [44] explored the potential energy landscape of screw dislocation motion in NbMoTaW RHEA that reveals a hierarchical and multilevel structure with a collection of small basins nested in large metabasin. We have also studied the effect of SRO on the dislocation nucleation and propagation in grain interiors and GBs of MoTaTiWZr RHEAs [45]. It was found that SRO was able to increase the energy barrier of edge dislocations more than that of screw dislocations, making the mobility of edge dislocations comparable to or even lower than screw dislocations, thus explaining the dominance of edge dislocations observed in BCC RHEAs [45]. To our knowledge, the effect of SRO on the dislocation activity at the crack tip of RHEAs has not been studied and reported.

Here, we perform hybrid MC/MD simulations to study the impacts of SRO on the dislocation activity at a crack tip in an equiatomic BCC MoTaTiWZr RHEA. Monte Carlo simulations are performed to exchange atoms of different types to obtain the energetically-favorable SRO, and MD is employed to both relax the atomic configuration and perform tensile deformation. The Warren-Cowley parameters [46] for all elemental pairs within the 1st to 3rd nearest neighbor shells are used to characterize SRO. MD simulations on the tensile deformation of MoTaTiWZr RHEAs with and without SRO are performed at room and elevated temperatures. The present work on the dislocation activities at the crack tip influenced by SRO at room and elevated temperatures will enable the development of RHEAs for structural applications.

2. Methods

In this section, we first validate the interatomic potential used in current study. Then, we present the initial atomistic model and hybrid MC/MD method to achieve SRO. Last, we discuss the parameters to characterize SRO and setting for tensile deformation.

2.1. Interatomic potential

The interatomic potential for the MoTaTiWZr RHEA is from Zhou et al. [47] embedded atom model (EAM) method, which is implemented in the large-scale atomic/molecular massively-parallel simulator (LAMMPS) package [48] and has been widely used to simulate MoTaTiWZr RHEAs [49,50]. DFT calculations are recognized for their accuracy in computing energetic data [51]. Utilizing this energetic data derived from DFT calculations as a benchmark to scrutinize the results of MD simulations offers a robust method for evaluating the precision of interatomic potentials. For example, Singh et al. [50] demonstrated that the structural parameters of $Mo_xTaTiWZr$ and $(MoW)_xTa_y(TiZr)_{1-x-y}$ obtained from this interatomic-potential-based MD agree well with those from DFT calculations. Besides, the temperature dependences of Young's moduli for commercial Mo-rich TiZrMo alloys obtained from MD simulations using this interatomic potential, DFT calculations, and experiments were also consistent [49]. Sharma et al. [50] compared the results from MD simulations at 77 K, using this interatomic potential and DFT calculations at 0 K for $(MoW)_{0.85}Zr_{0.075}(TaTi)_{0.075}$ and showed that the lattice constant, density, bulk modulus, and elastic constants all agree reasonably well.

We have further checked the validity of this interatomic potential by comparing the cohesive energies of B2 intermetallic and single-element BCC crystal structures in the MoTaTiWZr RHEA with DFT calculations [45]. The cohesive energies determined from the interatomic potentials used in the MD are remarkably successful in reproducing the important trends of DFT calculations [45]: (1) Ti-Ti exhibits the highest cohesive energy; (2) Mo-Zr and Mo-Mo possess medium cohesive energies; (3) Ta-W, Ta-Ta, and W-W have lower cohesive energies. Besides, we have also calculated and compared the stacking fault energy (SFE) and surface energy (SE) of RSS MoTaTiWZr RHEA [45]. The calculated values of MoTaTiWZr using MD interatomic potential are 0.8 J/m^2 (SFE) and 1.7 J/m^2 (SE), respectively [45]. These values are consistent with those in literature (SFE: 0.4–1.2 J/m^2 and SE: 1.5–2.5 J/m^2) [22,52]. Good agreements in these comparisons justify the use of the interatomic potential in the present study.

2.2. Model size and composition

The lattice constant of the BCC MoTaTiWZr RHEA was obtained after energy minimization at 0 K (3.29 Å). The simulation box was oriented with [112 ¯], [1 ¯10], and [111] directions aligned with *x, y* and *z* axes, respectively, whose dimension size was 10 × 30 × 10 nm^3. A near-equiatomic elemental composition was constructed by assigning atomic sites randomly with Mo, Ta, Ti, W, and Zr, i.e., 19.9 atomic percent (at.%) Mo, 20.1 at.% Ta, 20.0 at.% Ti, 20.0 at.% W, and 20.0 at.% Zr. The small deviations in the elemental compositions arise from the command "type/fraction" in LAMMPS to set the atom type for a fraction

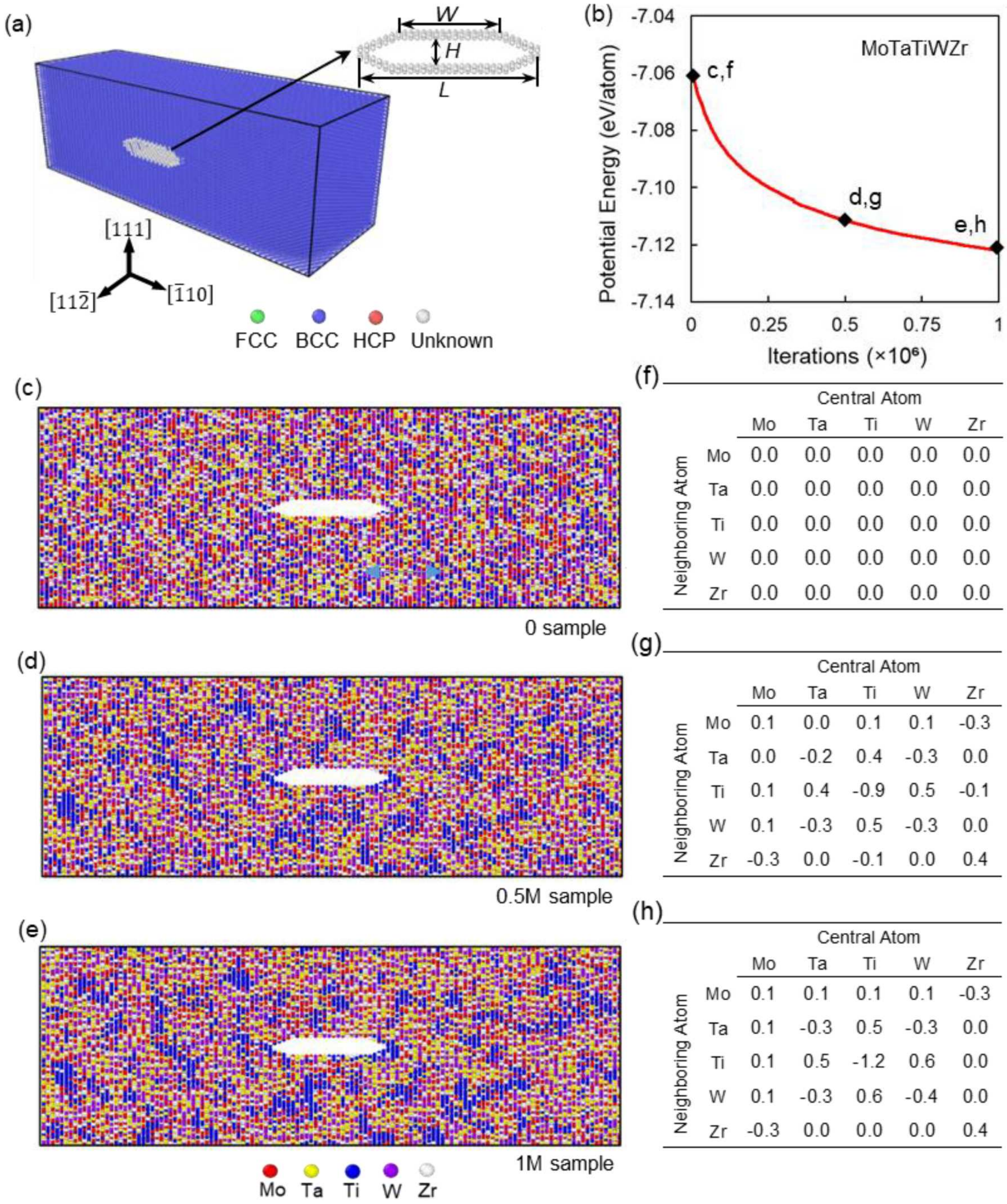

(f)

Neighboring Atom \ Central Atom	Mo	Ta	Ti	W	Zr
Mo	0.0	0.0	0.0	0.0	0.0
Ta	0.0	0.0	0.0	0.0	0.0
Ti	0.0	0.0	0.0	0.0	0.0
W	0.0	0.0	0.0	0.0	0.0
Zr	0.0	0.0	0.0	0.0	0.0

(g)

Neighboring Atom \ Central Atom	Mo	Ta	Ti	W	Zr
Mo	0.1	0.0	0.1	0.1	-0.3
Ta	0.0	-0.2	0.4	-0.3	0.0
Ti	0.1	0.4	-0.9	0.5	-0.1
W	0.1	-0.3	0.5	-0.3	0.0
Zr	-0.3	0.0	-0.1	0.0	0.4

(h)

Neighboring Atom \ Central Atom	Mo	Ta	Ti	W	Zr
Mo	0.1	0.1	0.1	0.1	-0.3
Ta	0.1	-0.3	0.5	-0.3	0.0
Ti	0.1	0.5	-1.2	0.6	0.0
W	0.1	-0.3	0.6	-0.4	0.0
Zr	-0.3	0.0	0.0	0.0	0.4

Fig. 1. Simulation model, potential energy, atomic configurations, and Warren-Cowley parameters of the MoTaTiWZr RHEA during iterations at 300 K. (a) Periodic BCC model oriented with [11$\bar{2}$], [$\bar{1}$10], and [111] directions aligned, respectively, along *x, y* and *z* axes, respectively. (b) Total potential energy as a function of the number of iterations. Atomic configurations colored according to elemental types and tables of Warren-Cowley parameters in the 1st-nearest neighbors at (c) and (f) 0 (0 sample), (d) and (g) 0.5 × 10^6 (0.5 M sample), and (e) and (h) 1 × 10^6 (1 M sample) iterations, as indicated in (b).

of atoms. Since uncertainties also exist in the experimental element concentrations, we decided not to correct those small deviations from the exact 20 at.% concentration value. Periodic boundary conditions were applied in all three directions. In order to investigate the influence of crystal orientations on the deformation mechanism, an additional simulation box is also constructed, where the $[1\bar{2}1]$, $[41\bar{2}]$, $[123]$ directions are aligned, respectively, with *x, y*, and *z* axes.

2.3. Atomic swap, relaxation, and crack

The elemental distribution in the MoTaTiWZr RHEA was optimized via MC swaps between atomic pairs at 300 K. The probability of each swap was evaluated as [53]

$$P = e^{-\frac{E(i+1)-E(i)}{kT}} \tag{1}$$

where k and T are the Boltzmann constant and temperature, respectively. The acceptance of each swap is determined by the Metropolis criterion [54]. If the probability (P) is not smaller than a uniformly-generated random number from (0, 1), the swap is accepted. Otherwise, it is rejected. The MC swaps were iterated with MD relaxations to converge elemental distributions and atomic distances. In this study, 100 MC swaps, followed by up to 100 MD relaxations per iteration were utilized since they showed good efficiency and accuracy. After 0.5×10^6 and 1×10^6 iterations, a crack with dimension size ($L = 6.5$ nm, $W = 3.7$ nm, and $H = 1.0$ nm in Fig. 1(a)) was created by removing the atoms within the crack dimension. Different samples were constructed with the crack in different atomic environments.

2.4. Characterization of short-range ordering

The Warren-Cowley parameters in the 1st- to 3rd-nearest neighbor shell were calculated to quantify SRO [46]:

$$W_{ijk} = 1 - N_{ijk} / \left(F_i N_{jk}\right) \tag{2}$$

where N_{ijk} is the number of i-type atoms in the kth-nearest neighbor of j-type atoms, N_{jk} is the total number of atoms in the kth-nearest neighbor of j-type atoms, and F_{i} is the atomic fraction of i-type atoms in the RHEA. If $W_{\mathrm{ijk}} < 0$, the i-j pairs are favorable. Otherwise, they are randomly distributed ($W_{\mathrm{ijk}} = 0$) or not favorable ($W_{\mathrm{ijk}} > 0$). The $\mathrm{k^{th}}$-nearest neighbors in the distorted structures are obtained by mapping to their perfect lattice structures without distortions.

2.5. Tensile deformation

The samples were thermally equilibrated in an isothermal-isobaric (NPT) ensemble for 0.2 ns with an integration time step of 1 fs by relaxing the pressures in three directions to zero. After that, uniaxial tensile deformation was performed in the z direction with a strain rate of $1 \times 10^8\ \mathrm{s}^{-1}$ at 300 K. During tensile deformation, the NPT ensemble was applied in the x and y directions to maintain zero lateral pressure. The evolution of atomic configurations was analyzed, using a dislocation extraction algorithm (DXA) [55] in OVITO [56].

3. Results

In this section, we first analyze the formation of SRO in the RHEA. Afterwards, we discuss the impact of SRO on dislocation nucleation at 300 K, where the effects of atomic environment of crack tip, crystal orientation, and crack dimension are carefully evaluated. Last, we explore the influence of SRO on dislocation activities, including the breakup, absorption, and annihilation of emitted dislocations and nucleation of new dislocations, at 1,200 K.

3.1. Short-range ordering in the MoTaTiWZr RHEA

The initially chemically random MoTaTiWZr RHEA simulation model is constructed by orienting a BCC box with $[11\bar{2}]$, $[\bar{1}10]$, and $[111]$ directions aligned, respectively, along *x, y*, and *z* axes. Hybrid MC swaps and MD relaxations run iteratively in the simulation box at 300 K to obtain energetically-favourable atomic configurations. The total potential energy per atom for the RHEA as a function of iteration is plotted in Fig. 1(b). The potential energy per atom at 0 (the 0 sample), 0.5×10^6 (the 0.5 M sample), and 1×10^6 (the 1 M sample) iterations is - 7.06, - 7.11, and - 7.12 eV/atom, respectively. After that, a crack is created at the center of 0, 0.5 M and 1 M samples, as shown in Fig. 1(a).

The atomic configurations colored according to the elemental type and corresponding Warren-Cowley parameters in the 1st-nearest neighbors (W_{ij1} in Eq. (2) in Methods section) for 0, 0.5 M, and 1 M samples are presented in Fig. 1(c–e) and (f–h), respectively. Fig. 1(c) and (f) show that the atoms in the 0 sample are randomly distributed in the 1st-nearest neighbors, and its W_{ij1} of all neighboring pairs are zero. Fig. 1(d)/(e) and (g)/(h) indicate that there is a strong tendency to form Ti-Ti pairs ($W =$ - 0.9/- 1.2) and, to a much lesser extent, W-W ($W =$ - 0.3/- 0.4), Mo-Zr ($W =$ - 0.3/- 0.3), Ta-W ($W =$ - 0.3/- 0.3), and Ta-Ta ($W =$ - 0.2/- 0.3) pairs in the 1st-nearest neighbors.

The Warren-Cowley parameters in the 2nd- and 3rd-nearest neighbors for the 0, 0.5 M, and 1 M samples are listed in Table 1. Table 1(a) and (d) show that the atoms in the 0 sample are randomly distributed in the 2nd- and 3rd-nearest neighbors (W_{ij2} and W_{ij3} are zero), which are similar to those in the 1st-nearest neighbors, forming an RSS. Table 1 (b)/(e) and (c)/(f) demonstrate that there is a similar tendency to form atomic pairs in the 2nd- and 3rd-nearest neighbors, as compared with that in the 1st-nearest neighbors.

The cohesive energies for 10 binary combinations of {Mo, Ta, Ti, W, and Zr} in the B2 intermetallic crystal structure and 5 single elements of {Mo, Ta, Ti, W, and Zr} in the BCC crystal structure [45] are listed in Table 2, indicating that Ti-Ti has the highest energy (- 4.9 eV/atom), and Ti-X ($X =$ Mo, Ta, W, or Zr) pairs have higher energies (- 6.5 to - 5.7 eV/atom). Besides, Mo-Mo (- 6.8 eV/atom) and Mo-Zr (- 7.0 eV/atom) are of medium energies, and W-W (- 8.8 eV/atom), Ta-W (- 8.4 eV/atom), and Ta-Ta (- 8.1 eV/atom) exhibit lower energies.

3.2. Impact of short-range ordering on dislocation nucleation at 300 K

Uniaxial tensile deformations were performed on the 0, 0.5 M, and 1 M samples at 300 K (the 0–300 K, 0.5M-300 K, and 1M-300 K samples) to study the impact of SRO on the dislocation activity at the crack tip in the MoTaTiWZr RHEA. The corresponding stress-strain curves are shown in Fig. 2(a). The results indicate that there are no dislocations observed prior to the ultimate tensile strength (UTS) in the 0–300 K, 0.5M-300 K, and 1M-300 K samples. Fig. 2(b–d) shows the dislocation structures of these three samples at the UTS according to the DXA [55] in OVITO [56], indicating that dislocation nucleation from the crack tip dominates the UTS in both RSS (0–300 K) and SRO (0.5M-300 K and 1M-300 K) samples. The dislocation types in Fig. 2(b–d) are enlarged in Fig. 2(e–g), respectively. Clearly, all the nucleated dislocations in these three samples have a Burgers vector of $1/2\ \langle 111 \rangle$, which indicates that they are full dislocations with screw and edge characters. These full dislocations lie on the {112}-type slip planes (Schmid factor: 0.314) in the 0–300 K sample and {123}-type slip planes (Schmid factor: 0.309) in the 0.5M-300 K and 1M-300 K samples. Following the UTS, dislocation propagation occurs in these three samples.

To reveal the effect of SRO on dislocation nucleation in the MoTaTiWZr RHEA, we define three different energy clusters according to their local atomic environment. Chemical-affinity disparity and exclusivity lead to the formation of SRO [40]. The chemical affinity is intrinsically related to the cohesive energy of atomic pairs, where high/medium/low cohesive energy corresponds to weak/medium/strong chemical affinity,

Table 1
Warren-Cowley parameters in the 2nd- and 3rd-nearest neighbors at (a) and (d) 0 (0 sample), (b) and (e) 0.5 × 10^6 (0.5 M sample), and (c) and (f) 1 × 10^6 (1 M sample) iterations.

(a)

		Central Atom				
		Mo	Ta	Ti	W	Zr
Neighboring Atom	Mo	0	0	0	0	0
	Ta	0	0	0	0	0
	Ti	0	0	0	0	0
	W	0	0	0	0	0
	Zr	0	0	0	0	0

(b)

		Central Atom				
		Mo	Ta	Ti	W	Zr
Neighboring Atom	Mo	0.3	−0.2	−0.1	0.3	−0.3
	Ta	−0.2	0	0.3	−0.4	0.2
	Ti	−0.1	0.3	−0.8	0.4	0.1
	W	0.3	−0.4	0.4	0.1	−0.4
	Zr	−0.3	0.2	0.1	−0.4	0.3

(c)

		Central Atom				
		Mo	Ta	Ti	W	Zr
Neighboring Atom	Mo	0.3	−0.2	−0.1	0.4	−0.5
	Ta	−0.2	0	0.4	−0.6	0.3
	Ti	−0.1	0.4	−1.1	0.5	0.2
	W	0.4	−0.6	0.5	0.1	−0.5
	Zr	−0.5	0.3	0.2	−0.5	0.4

(d)

		Central Atom				
		Mo	Ta	Ti	W	Zr
Neighboring Atom	Mo	0	0	0	0	0
	Ta	0	0	0	0	0
	Ti	0	0	0	0	0
	W	0	0	0	0	0
	Zr	0	0	0	0	0

(e)

		Central Atom				
		Mo	Ta	Ti	W	Zr
Neighboring Atom	Mo	−0.1	0.1	0	−0.1	0.2
	Ta	0.1	−0.1	0.1	0	−0.1
	Ti	−0.1	0.1	−0.3	0.2	0
	W	−0.1	0	0.2	−0.2	0.1
	Zr	0.2	−0.1	0.1	0.1	−0.1

(f)

		Central Atom				
		Mo	Ta	Ti	W	Zr
Neighboring Atom	Mo	−0.3	0.2	−0.1	−0.2	0.2
	Ta	0.2	−0.2	0.2	0.1	−0.2
	Ti	0	0.2	−0.6	0.3	0.1
	W	−0.2	0.1	0.3	−0.4	0.2
	Zr	0.3	−0.2	0.1	0.2	−0.3

Table 2
Cohesive energies of the B2 intermetallic crystal structure and single elements in the BCC crystal structure for the MoTaTiWZr RHEA. Unit: eV/atom [45].

	Mo	Ta	Ti	W	Zr
Mo	−6.8	−7.5	−5.8	−7.8	−7.0
Ta	−7.5	−8.1	−6.3	−8.4	−7.3
Ti	−5.8	−6.3	−4.9	−6.5	−5.7
W	−7.8	−8.4	−6.5	−8.8	−7.7
Zr	−7.0	−7.3	−5.7	−7.7	−6.3

respectively. The chemical affinities of W-W (−8.8 eV/atom), Ta-W (−8.4 eV/atom), and Ta-Ta (−8.1 eV/atom) are very strong, contributing to the formation of SRO between W and Ta. Therefore, if the concentrations of Ta and W are higher than those of Mo, Ti, and Zr within the second nearest neighbour of a particular atom, it belongs to a low-energy cluster (LEC). Similarly, Ti-X (X = Mo, Ta, W, or Zr) pairs have higher energies (- 6.5 to - 5.7 eV/atom). Therefore, if the Ti concentration in the atomic environment is larger than the concentration of any of the other four elements, it belongs to a high-energy cluster (HEC). Of course, the atom belongs to a medium-energy cluster (MEC) if it does not belong to LEC and HEC.

Using the first-dislocation-nucleation site as a center, the simulation box is cut into multiple spherical shells with 1 Å thickness along the radial direction. The atomic fractions of different energy clusters (HEC, MEC, and LEC) in these spherical shells as a function of distance from the center in the 0–300 K, 0.5M-300 K, and 1M-300 K samples are plotted in Fig. 3(a–c), respectively. The spatial distributions for HECs, MECs, and LECs in these three samples are also drawn in Fig. 3(d–f), where the white-dotted circles denote dislocation-nucleation sites. Clearly, dislocation nucleation is highly correlated with Ti-rich HECs, particularly in the 0.5M-300 K and 1M-300 K samples. Since Ti is intrinsically stable in a hexagonal-close-packed (HCP) structure at room temperature [57], Ti-rich HECs tend to transform from BCC to HCP structures under tension at 300 K. Therefore, HECs are less stable and more favorable to generate dislocations than MECs and LECs during tensile deformation.

To further verify the effect of SRO at the crack tip on the dislocation nucleation in MoTaTiWZr RHEAs, we have created another two same-sized cracks with different atomic environments from that in Fig. 2 (shown in Fig. 4). One set of cracks are created right below (2 nm distance) that in Fig. 2 (denoted as 0′, 0.5 M’ and 1M’ samples, as shown in Fig. 4(a–c)), while the other set of cracks are right above (2 nm distance) that in Fig. 2 (denoted as 0’’, 0.5 M’’ and 1M’’ samples, as shown in Fig. 4(d–f)). We performed tension simulations on these two sets of samples at the same temperature of 300 K (denoted as the 0′-300 K, 0.5M’−300 K and 1M’−300 K samples, and the 0′’−300 K, 0.5M’’−300 K, and 1M’’−300 K samples, respectively).

Figs. 5 and 6 show the simulation results for these two sets of samples, respectively. The stress-strain curves in Figs. 5(a)/6(a) and dislocation structures in Figs. 5(b–d)/6(b–d) confirm that the UTS of MoTaTiWZr RHEAs is dominated by dislocation nucleation. Figs. 5(e–g)/6(e-g) verify that Ti-rich HECs are favorable for dislocation nucleation. The radii of the Ti-rich HECs at the dislocation-nucleation sites are in the range from 4 (Figs. 3(b)/(c)/6(f)) to 8 Å (Figs. 5(f)/(g)/6(g)). The spatial distributions of different energy clusters also indicate that the HECs are surrounded by MECs (a distance of 4 – 12 Å from the dislocation nucleation site in Fig. 3(b) and (c)). Hence, MECs serve as a strong matrix to stabilize the HECs, and the dislocation nucleation in HECs are delayed by MECs.

To further explore the influence of crystal orientation on the deformation mechanism in MoTaTiWZr RHEAs, we have constructed one more set of samples with different crystal orientations compared to those in Fig. 2 (the [111] case). These new samples are oriented with $[1\bar{2}1]$, $[41\bar{2}]$, and [123] directions, which are aligned, respectively, with x, y, and z axes (the [123] case). The stress-strain curves in Fig. 7(a) and dislocation structures in Fig. 7(b–d) demonstrate that the deformation mechanism of the [123] case is consistent with that of the [111] case, i.e., UTS is governed by dislocation nucleation at the crack tip. Besides, we have created a sharp crack in the 0, 0.5 M, and 1 M samples by eliminating the interactions between two neighboring layers instead of removing atoms (denoted as 0-Sharp, 0.5M-Sharp, and 1M-Sharp). The atomic configurations of the 0-Sharp sample at a 2 % strain colored

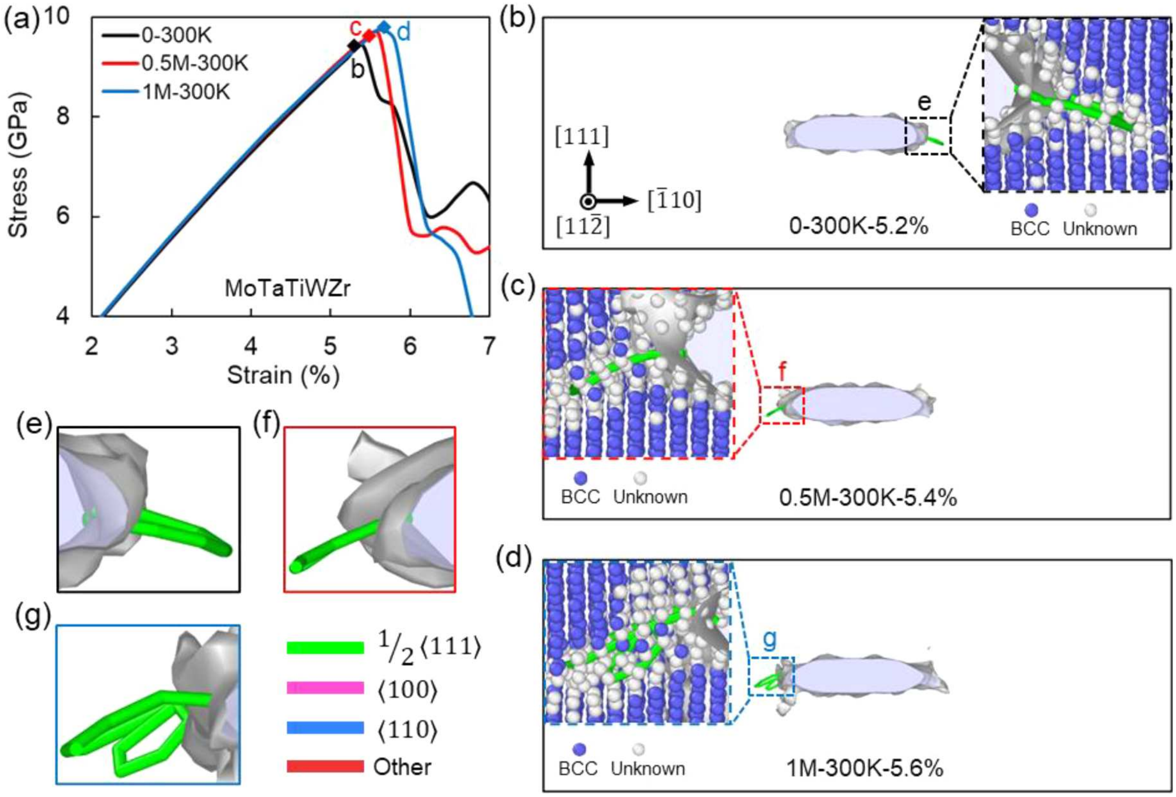

Fig. 2. Stress-strain curves and dislocation structures of the MoTaTiWZr RHEA at 300 K. (a) Stress as a function of strain for the samples after 0 (0–300 K), 0.5 × 10^6 (0.5M-300 K), and 1 × 10^6 (1M-300 K) iterations upon uniaxial tension at 300 K. Dislocation structures at the ultimate tensile strength: (b) 0–300 K sample at a 5.2 % strain (e enlarged image), (c) 0.5M-300 K sample at a 5.4 % strain (f enlarged image), and (d) 1M-300 K sample at a 5.6 % strain (g enlarged image), as indicated in (a).

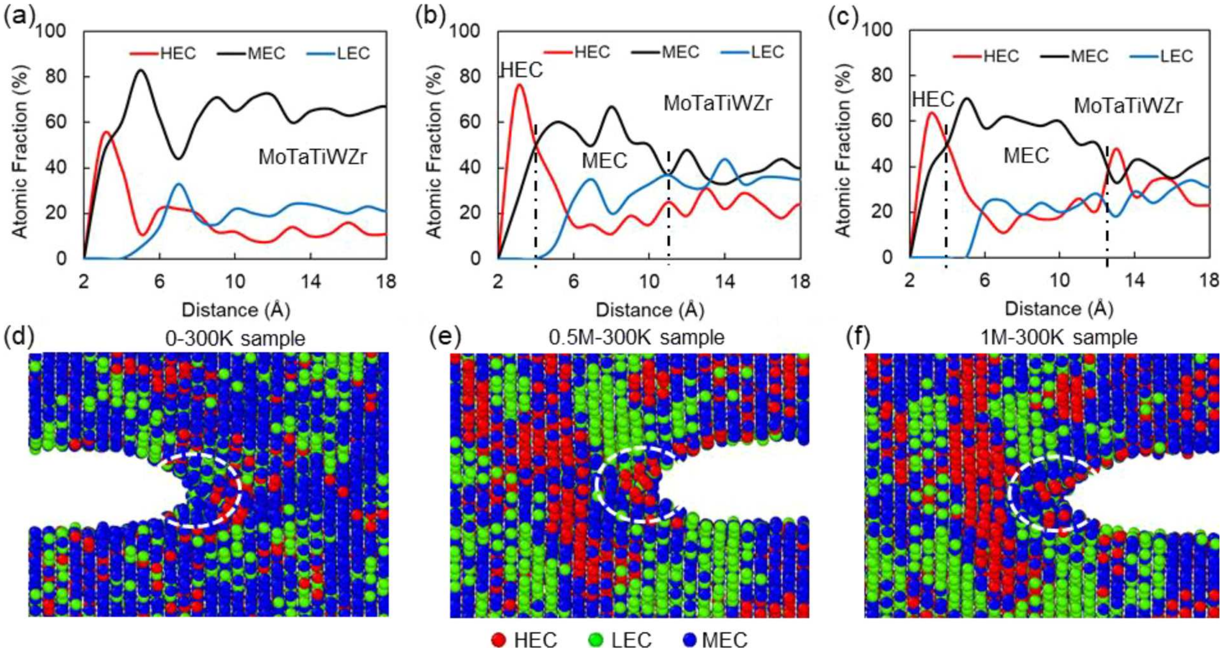

Fig. 3. Atomic fractions of different energy clusters as a function of the distance from the dislocation-nucleation site and spatial distributions of different energy clusters in the MoTaTiWZr RHEA. Atomic fractions of different energy clusters (HEC, MEC, and LEC) as a function of the distance from the dislocation-nucleation site in (a) the 0–300 K sample, (b) the 0.5M-300 K sample, and (c) the 1M-300 K sample. Spatial distributions of HECs, MECs, and LECs for (d) the 0–300 K sample, (e) the 0.5M-300 K sample, and (f) the 1M-300 K sample. White dotted circles denote the dislocation-nucleation sites.

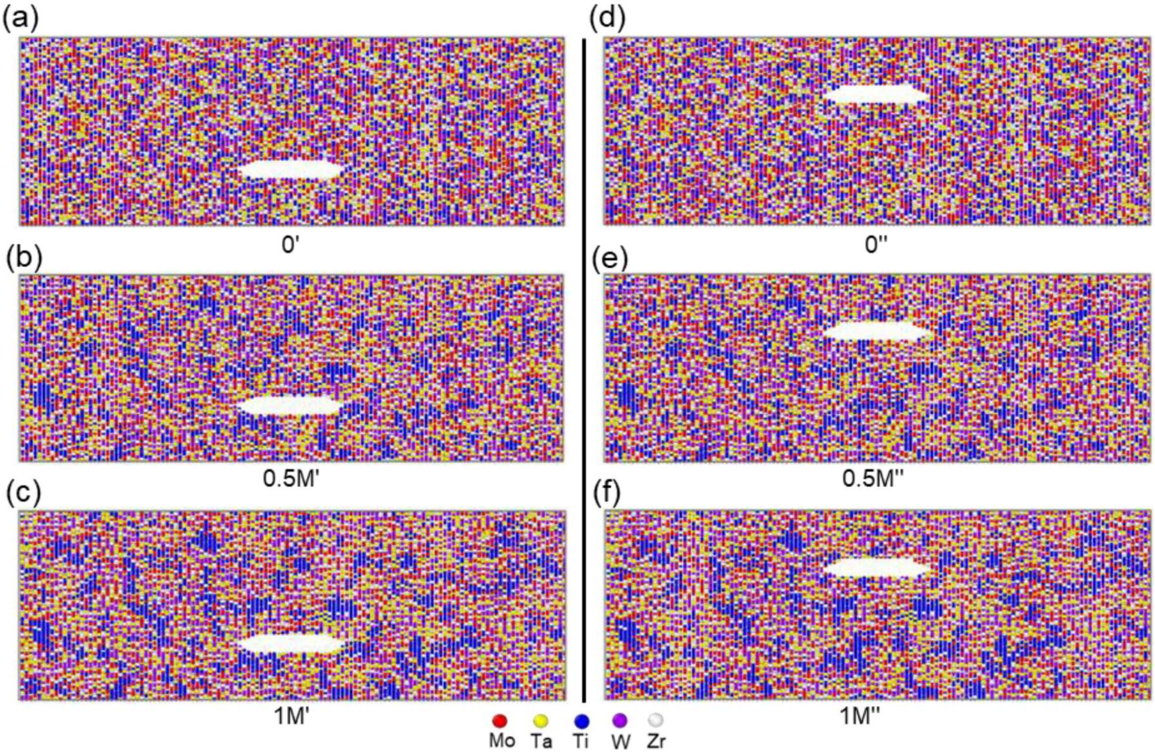

Fig. 4. Atomic configurations of the MoTaTiWZr RHEA with the same-sized cracks but in different atomic environments from that in Fig. 2. The samples after (a) 0 (0′), (b) 0.5 × 10^{6} (0.5M’), and (c) 1 × 10^{6} (1M’) iterations with a crack in a different atomic environment from that in Fig. 2. The samples after (d) 0 (0′’), (e) 0.5 × 10^{6} (0.5M’’), and (f) 1 × 10^{6} (1M’’) iterations with a crack in a different atomic environment from those in Fig. 2 and (a–c).

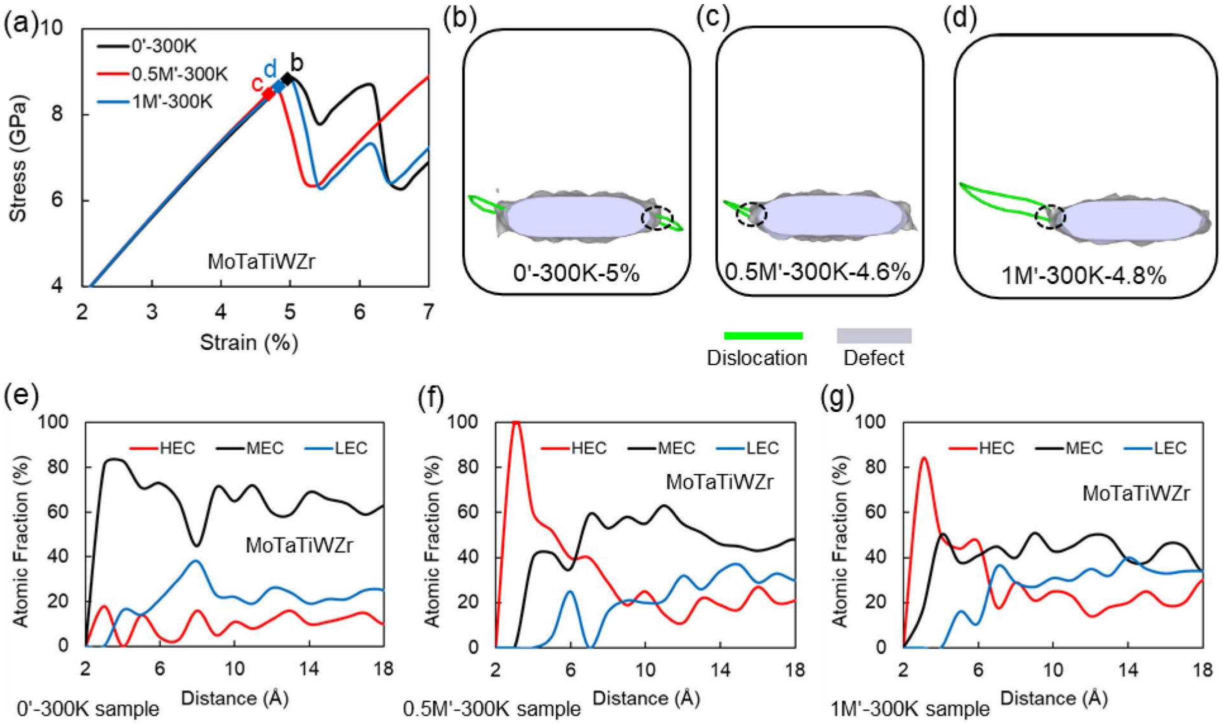

Fig. 5. Stress-strain curves, dislocation structures, and atomic fractions of different energy clusters as a function of the distance from the dislocation-nucleation site of the MoTaTiWZr RHEA with a crack in a different atomic environment from that in Fig. 2 during tension at 300 K. (a) Stress as a function of the strain for the samples after 0 (0′-300 K), 0.5 × 10^{6} (0.5M’−300 K), and 1 × 10^{6} (1M’−300 K) iterations with a crack in a different atomic environment from that in Fig. 2 during tension at 300 K. Dislocation structures of (b) 0′-300 K sample at a 5 % strain, (c) 0.5M’−300 K sample at a 4.6 % strain, and (d) 1M’−300 K sample at a 4.8 % strain, as indicated in (a). Black-dotted circles denote the dislocation-nucleation sites. Atomic fractions of different energy clusters as a function of the distance from the dislocation-nucleation site in (e) the 0′-300 K sample, (f) the 0.5M’−300 K sample, and (g) the 1M’−300 K sample.

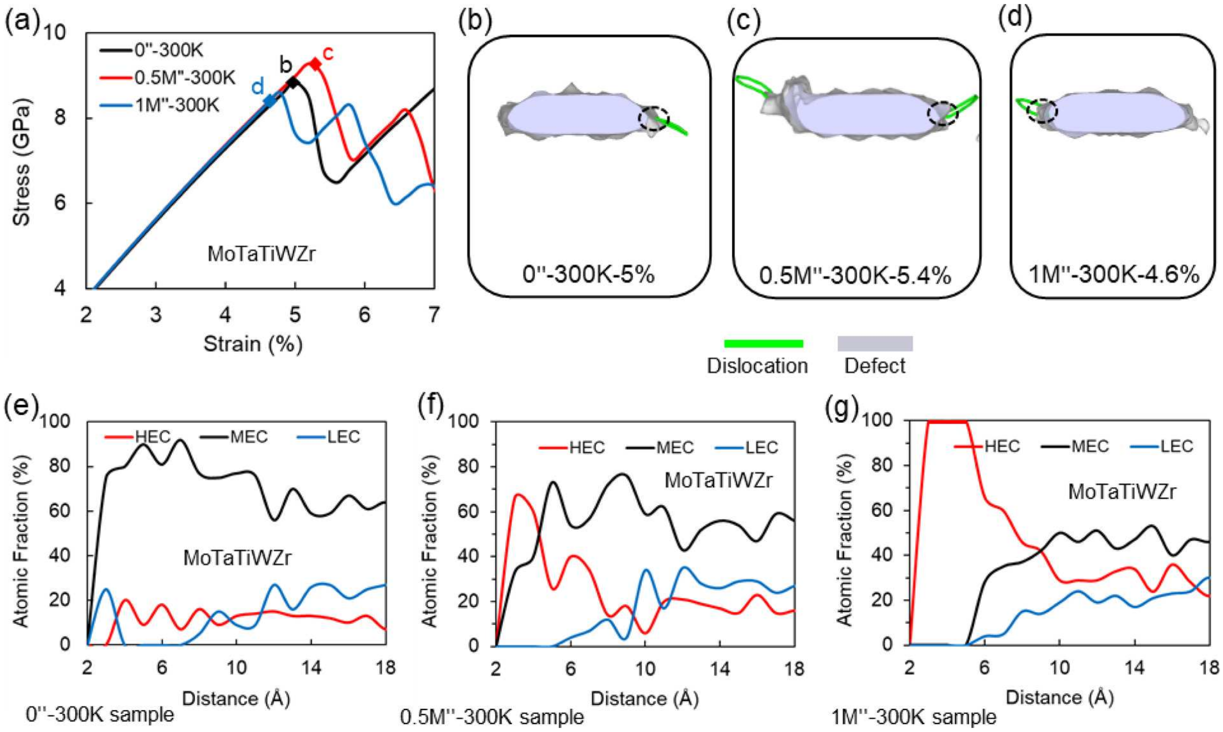

Fig. 6. Stress-strain curves, dislocation structures, and atomic fractions of different energy clusters as a function of the distance from the dislocation-nucleation site of the MoTaTiWZr RHEA with a crack in a different atomic environment from those in Figs. 2 and 4(a-c) during tension at 300 K. (a) Stress as a function of the strain for the samples after 0 (0’’−300 K), 0.5 × 10^6 (0.5M’’−300 K), and 1 × 10^6 (1M’’−300 K) iterations with a crack in a different atomic environment from those in Figs. 2 and 4(a-c) during tension at 300 K. Dislocation structures of (b) the 0’’−300 K sample at a 5 % strain, (c) the 0.5M’’−300 K sample at a 5.4 % strain, and (d) the 1M’’−300 K sample at a 4.6 % strain, as indicated in (a). Black-dotted circles denote the dislocation-nucleation sites. Atomic fractions of different energy clusters as a function of the distance from the dislocation-nucleation site in (e) the 0’’−300 K sample, (f) the 0.5M’’−300 K sample, and (g) the 1M’’−300 K sample.

according to atom type and phase structure are shown in Fig. 8(a) and (b), respectively. The stress-strain curves in Fig. 8(c) and dislocation structures in Fig. 8(d-e) indicate that the deformation mechanisms in the samples with a sharp crack (the 0-Sharp, 0.5M-Sharp, and 1M-Sharp samples) are consistent with those in the 0, 0.5 M, and 1 M samples, i.e., UTS is governed by dislocation nucleation at the crack tip.

3.3. Impact of short-range ordering on dislocation activities at 1200 K

To explore the impact of SRO on the dislocation activity at elevated temperature, we performed uniaxial tensile deformations on the 0, 0.5 M, and 1 M samples at 1,200 K (the 0–1200 K, 0.5M-1200 K, and 1M-1200 K samples). The corresponding stress-strain curves in Fig. 9(a) indicate that there are several stress peaks and valleys from a 4 % to 7 % strain, which are quite different from those in Fig. 2(a) with only one stress peak (UTS). Besides, for the 0.5M-1200 K sample, the subsequent stress peak at a 7 % strain is higher than the initial one, i.e., strain hardening. To reveal the origin of these stress peaks and valleys at 1,200 K, we have further analyzed the dislocation structures at different strains (shown in Fig. 9(b–i)).

Fig. 9(b) (with dislocations) and (c) (without dislocations) show the structures of the 0–1200 K sample at a 4.4 % strain (stress peak) and a 4.6 % strain (stress valley), respectively. Clearly, the stress reaches the peak at a 4.4 % strain once dislocation nucleation occurs, while the stress arrives at the valley at a 4.6 % strain once dislocation annihilation takes place. Similarly, Fig. 9(e) (with dislocations), (f) (without dislocations), (g) (with dislocations), (h) (without dislocations), and (i) (with dislocations) draw the structures of the 0.5M-1200 K sample at a 4.3 % strain (stress peak), 4.5 % strain (stress valley), 5 % strain (stress peak), 5.2 % strain (stress valley), and 7 % strain (stress peak), respectively. These results in the 0.5M-1200 K sample further verify that the stress peaks and valleys correspond to the dislocation nucleation and annihilation. Therefore, dislocation nucleation occurs at the UTS and also at the subsequent stress peaks posterior to the UTS. The dislocation nucleation in the 0.5M-1200 K sample is similar to that in the 0.5M-300 K sample, while dislocation annihilation marks the major difference between the 0.5M-1200 K and 0.5M-300 K samples.

To understand the dislocation nucleation and annihilation processes, we have further analysed the local dislocation and phase (BCC and defect) structures of the 0.5M-1200 K sample (Fig. 10). Defect structures are those atoms identified as unknown using DXA [55] in OVITO [56]. Fig. 10(a–f) indicates that the defect structures facilitate the formation of two dislocation loops (a 5.13 % strain in Fig. 10(c)) and further absorb the dislocations (a 5.133 % strain in Fig. 10(d) and 5.135 % strain in Fig. 10(e)), subsequently resulting in the dislocation annihilation (a 5.14 % strain in Fig. 10(f)). Fig. 10(g–k) demonstrates that the defect structures are comprised of two types of configurations. One of them still follows the BCC lattice but has severe lattice distortions (bond length ranges from 2.8 Å to 4.7 Å, as shown in Fig. 10(k)), as compared with the BCC structure with a normal lattice distortion (identified as a BCC phase using DXA [55] in OVITO [56], bond length ranges from 2.9 to 3.7 Å in Fig. 10(g)). The other one is disordered, as presented in Fig. 10(h–j), where the atoms are not located in the normal FCC/BCC/HCP lattice sites.

Fig. 11(a) plots the ratio of defect structures, i.e., the number of atoms in amorphous structures divided by the total number of atoms, as a function of strain at 300 K and 1200 K. These results demonstrate that the samples at 1,200 K contain much more defect structures than those at 300 K, and the ratio of defect structures increases dramatically with strain at 1,200 K. The trends indicate that transformations from BCC lattices to defect structures are energetically more favorable during tension at elevated temperatures. Elemental concentrations of defect structures in the 0.5M-1200 K sample under 6 % strain are shown in Fig. 11(b). It is seen that Ti and Zr are dominant in the defect structures,

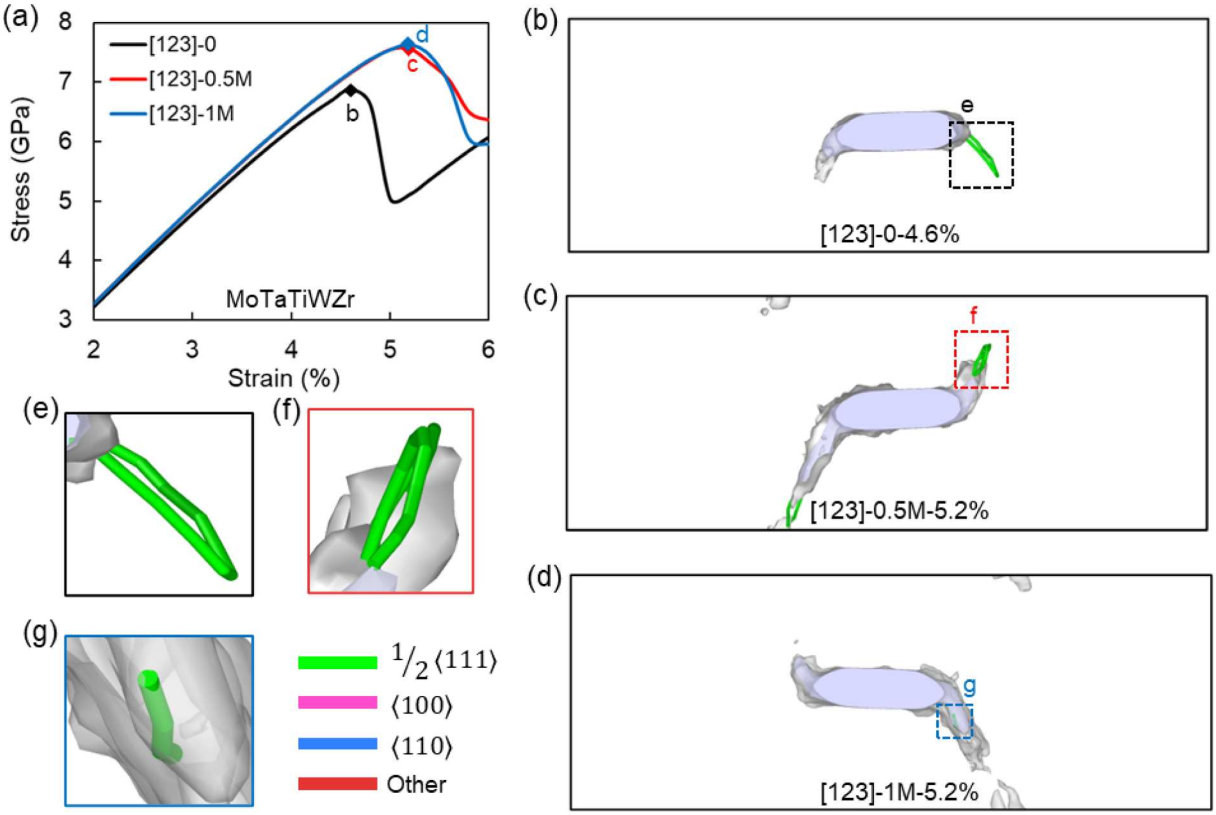

Fig. 7. Stress-strain curves, dislocation structures, and phase structures of the MoTaTiWZr RHEA with different crystal orientations compared to those in Fig. 2 during tension at 300 K. (a) Stress as a function of strain for the MoTaTiWZr RHEA oriented with [1$\bar{2}$1], [41$\bar{2}$], and [123] directions, which are aligned, respectively, with *x, y*, and *z* axes after 0 ([123]−0), 0.5 × 10^6 ([123]−0.5 M), and 1 × 10^6 ([123]−1 M) iterations during tension at 300 K. Dislocation structures of (b) the [123]−0 sample at a 4.6 % strain (e enlarged image), (c) the [123]−0.5 M sample at a 5.2 % strain (f enlarged image), and (d) the [123]−1 M sample at a 5.2 % strain (g enlarged image), as indicated in (a).

i.e., HECs.

The dislocation characteristics and defect structures of the 0.5–1200 K sample at different strains are shown in Fig. 12(a–f). Fig. 12(a) indicates that the nucleated dislocation at a 5.1 % strain is screw-character dominated and has a Burgers vector of 1/2[111]. During further tension, defects (that is, severely distorted BCC and disordered phases) are formed ahead of the crack tip, causing the dislocation to break up into two connecting loops (a 5.13 % strain in Fig. 12(b), the connecting configurations are edge- and mixed-character dominated). Subsequently, when the defects are sufficiently large, the two dislocation loops are separated apart (a 5.135 % strain in Fig. 12(c)). Further tension causes the defect expansion and the absorption and annihilation of the dislocation loop near the crack tip (a 5.14 % strain in Fig. 12(d)). It is noted that these defects can also serve as a favorable location for the nucleation of new dislocations with screw and mixed characters (a 6.41 % strain in Fig. 12(e)). After nucleation, the dislocations can even propagate towards the crack tip (a 6.45 % strain in Fig. 12(f)).

4. Discussion

In this section, we first discuss the rationality of formation of Ti-rich HECs via SRO and compare our results with those in literature. Then, we analyze the underlying mechanism for dislocation reactions in HEAs with SRO. Last, we propose possible strategy for exploiting SRO in the design of RHEA.

4.1. Formation of Ti-rich HECs in the MoTaTiWZr RHEA

In the BCC MoTaTiWZr RHEA, the Warren-Cowley parameters and atomic configurations in Fig. 1 demonstrate the formation of Ti-rich HECs via SRO. These Ti-rich HECs play a dominant role in dislocation activities, including the nucleation of dislocations at the crack tip (resulting from the transformation from BCC to HCP structures) and the breakup, absorption, and annihilation of dislocations near the crack tip (induced by the transformations to severely-distorted BCC and disordered structures). It is understood that the BCC Ti is thermodynamically unstable at low temperatures according to its phase diagram [57]. Therefore, the Ti-rich HECs are presumably stabilized by other elements (Mo, Ta, W, and Zr) in the RHEAs. Elemental concentrations of defect structures in Fig. 11(b) ($Mo_{19}Ta_{12}Ti_{31}W_{13}Zr_{25}$) show the formation of (Ti, Zr)-rich regions, i.e., Ti is stabilized by Zr. This trend has also been observed in other experiments and simulations. For example, Lei et al. [58] observed the existence of (Ti, Zr)-rich regions in TiZrHfNb, using an aberration-corrected scanning transmission electron microscope. In the same alloy, Zhang et al. [59] revealed the preference for Ti-Zr and Nb-Hf environments, employing DFT-based MC simulations. Xun et al. [60] also found (Ti, Zr)-rich regions in TiZrNb, TiZrHfNb, and TiZrHfNbTa using a cluster-expansion approach. Ti could also be stabilized by Ta [61,62], Mo [63], and W [64] in the BCC structure according to their phase diagrams.

In addition to the formation of the Ti-rich HECs via SRO, (W, Ta)-rich LECs have also been formed. It is expected that (W, Ta)-rich LECs play an important role in stabilizing the HEAs by supressing or delaying the defect and dislocation nucleation and propagation. The formation of W-Ta pairs has also been observed by Sobieraj et al. [65] in CrTaVW, $Ti_{0.04}(CrTaVW)_{0.96}$, and $Ti_{0.07}(CrTaVW)_{0.93}$, using an ab-initio-based cluster expansion Hamiltonian model in combination with MC simulations. Even though currently there is no experimental work on SRO of MoTaTiWZr RHEAs, the above literature results provide evidence that supports our findings.

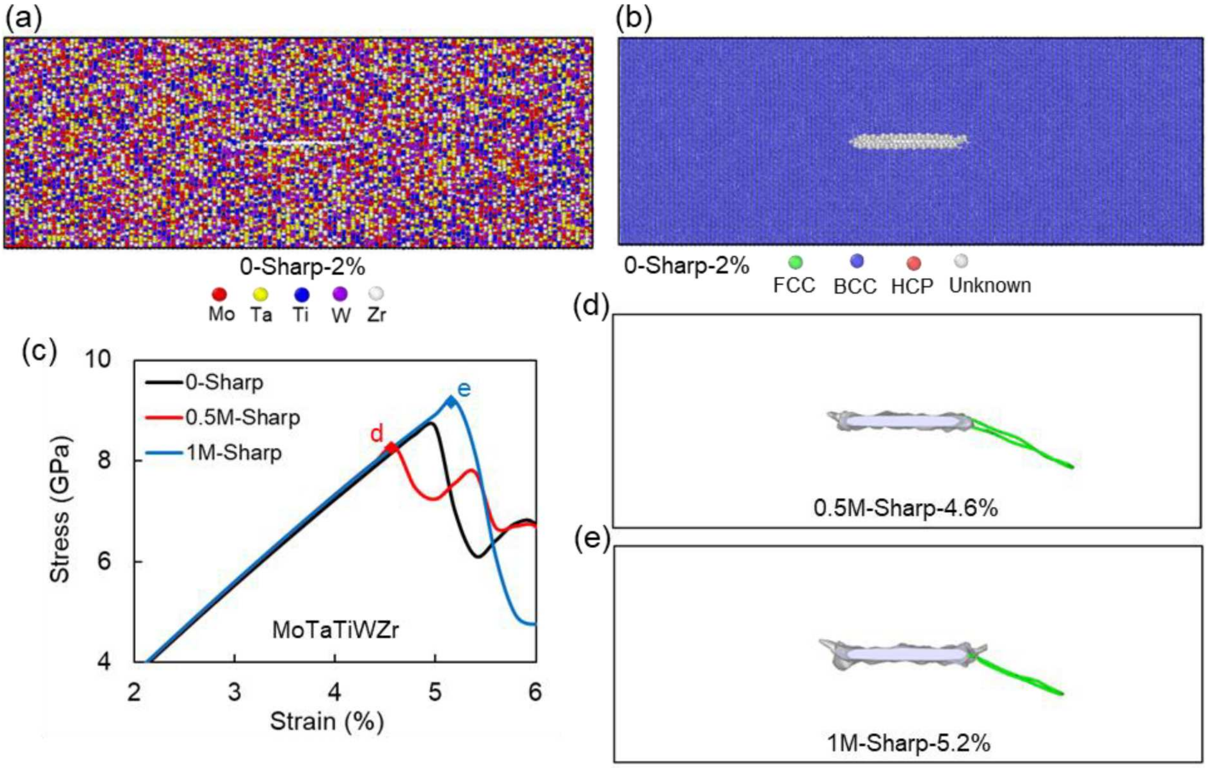

Fig. 8. Atomic configurations and stress-strain curves of the MoTaTiWZr RHEA with a sharp crack during tension at 300 K. Atomic configurations of the 0 sample with a sharp crack (0-Sharp) by eliminating the interactions between two neighboring layers instead of removing atoms at a 2 % strain colored according to (a) atom type and (b) phase structure. (c) Stress as a function of the strain for the 0-Sharp sample, and the 0.5 M and 1 M samples with a sharp crack (0.5M-Sharp and 1M-Sharp). Dislocation structures of (d) the 0.5M-Sharp sample at a 4.6 % strain, and (e) the 1M-Sharp sample at a 5.2 % strain, as indicated in (c).

4.2. Mechanism of dislocation reactions

Fig. 10 indicates that a dislocation breakup occurs in the BCC MoTaTiWZr RHEA at 1,200 K due to the formation of severely distorted BCC and disordered phases ahead of the crack tip. The formation of these defects can also promote the absorption and annihilation of these dislocations. After the breakup, absorption, and annihilation of these dislocations, stress starts to increase again. Therefore, the dislocation breakup, absorption, and annihilation due to the defect formation ahead the crack tip play a significant role in improving the mechanical properties of the RHEA at elevated temperatures. A similar process has also been observed experimentally. For example, Li et al. [66] investigated the dislocation activities in FeCoCr at 700 °C during experimental compressive loading and proposed the conditions for dislocation reactions, i.e., dislocations with opposite signs meet when the distance of adjacent dislocations is less than a critical value. However, in our BCC MoTaTiWZr RHEA, the dislocation breakup, absorption, and annihilation are associated with the transformations of Ti-rich HECs from normally distorted BCC to severely distorted BCC and disordered structures ahead the crack tip during tension at elevated temperatures.

4.3. Strategy for exploiting SRO in the RHEA design

Typical strengthening strategies in the HEA design involve forming stable and strong SRO or nanoprecipitates [67], i.e., LECs. For example, Ding et al. [24] fabricated an FCC CoCrFeNiPd HEA with remarkable elemental aggregation in 1–3 nm sizes, leading to considerable resistance to dislocation glide and enhancing the yield strength with comparable strain hardening, as compared to CoCrFeNiMn with little elemental aggregation. However, in the MoTaTiWZr RHEA described above, tuning the mechanical property can be achieved by the manipulation of the HECs.

We propose that instead of designing SRO or nanoprecipitates to prohibit dislocation glide, RHEAs may be designed to delay dislocation nucleation and/or induce dislocation breakup, absorption, and annihilation via controlling the HECs. For example, in a five-element HEA, several elements-rich regions may form stable LECs/MECs via SRO, while the other elements-rich regions may form less stable HECs. The weak HEC fillers can be stabilized by the strong MEC matrix and LEC clusters, thus delaying the dislocation nucleation. For the HECs located near the crack tip, they may undergo phase transformations, which in turn can cause the dislocation breakup, absorption, and annihilation. In such an HEA with a pseudo-composite microstructure via SRO, the strength and ductility are likely to be enhanced during deformation via delaying the dislocation nucleation and/or causing the dislocation breakup, absorption, and annihilation.

5. Conclusions

In summary, we perform iterative MC and MD simulations to obtain energetically favorable SRO in the BCC MoTaTiWZr RHEA, and then by introducing a crack, we perform MD simulations to explore the effect of SRO on the dislocation activities at the crack tip in the RHEA. The results demonstrate that the formation of SRO is energetically favorable in the RHEA, leading to a pseudo-composite microstructure with LECs, MECs, and HECs. At room temperature, the HECs at the crack tip act as weak fillers to induce dislocation nucleation via transformation from BCC to HCP structures, while the MECs serve as a strong BCC matrix to stabilize the weak HECs. At elevated temperatures, the HECs near the crack tip tend to transform to severely distorted BCC and disordered structures, which cause the breakup, absorption, and annihilation of emitted dislocations and nucleation of new dislocations with screw and mixed characters. The present study not only reveals the complex role of SRO in governing the dislocation activities in the crack tip of RHEAs, but also

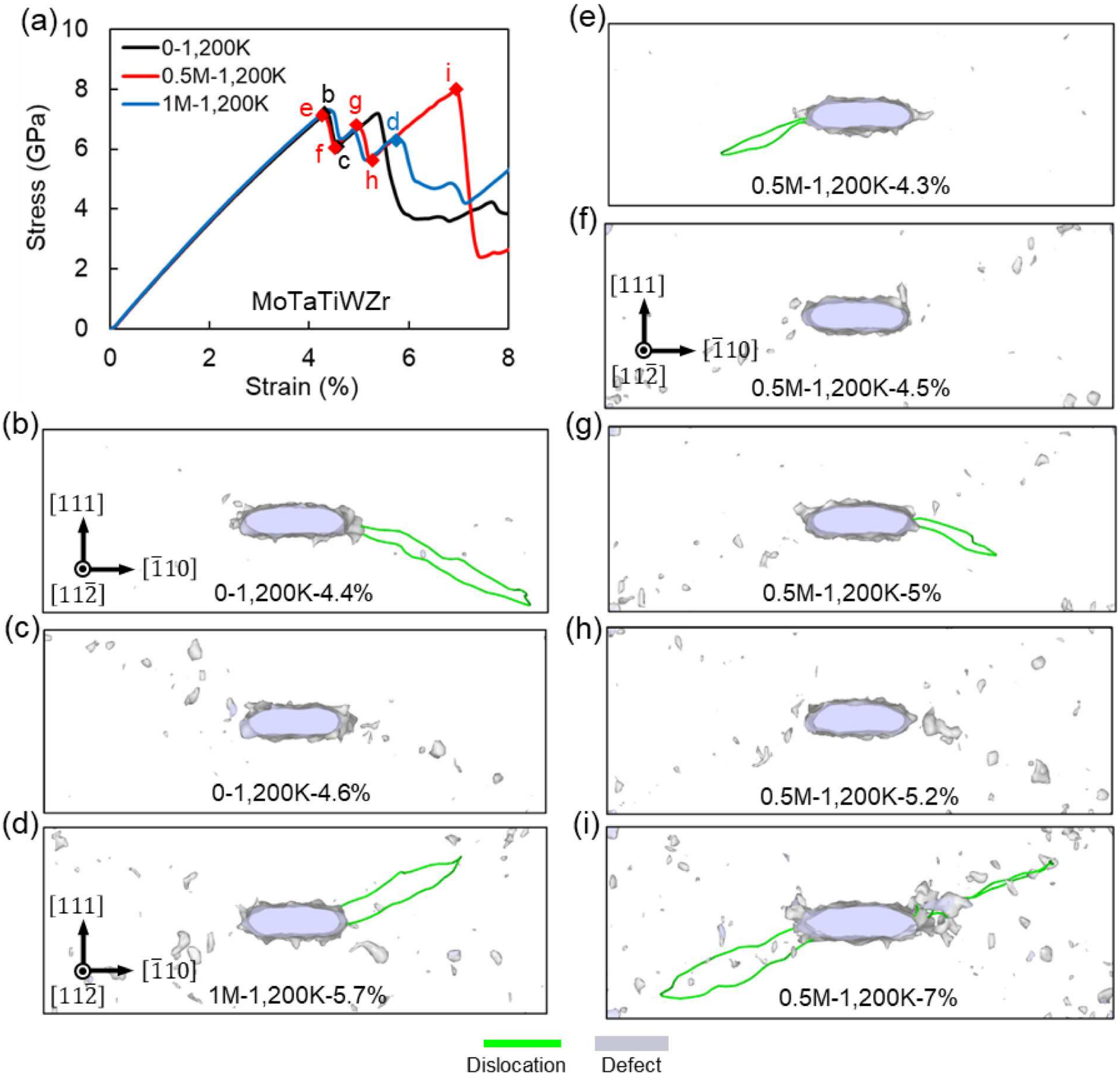

Fig. 9. Stress-strain curves and dislocation structures of the MoTaTiWZr RHEA at 1,200 K. (a) Stress as a function of strain for the samples after 0 (0–1200 K), 0.5 × 10^6 (0.5M-1200 K), and 1 × 10^6 (1M-1200 K) iterations during tension at 1,200 K. Dislocation structures of 0–1200 K sample at (b) 4.4 % strain and (c) 4.6 % strain, (d) 1M-1200 K sample at a 5.7 % strain, and 0.5M-1200 K sample at (e) 4.3 % % strain, (f) 4.5 % strain, (g) 5 % strain, (h) 5.2 % strain, and (i) 7 % strain, as indicated in (a).

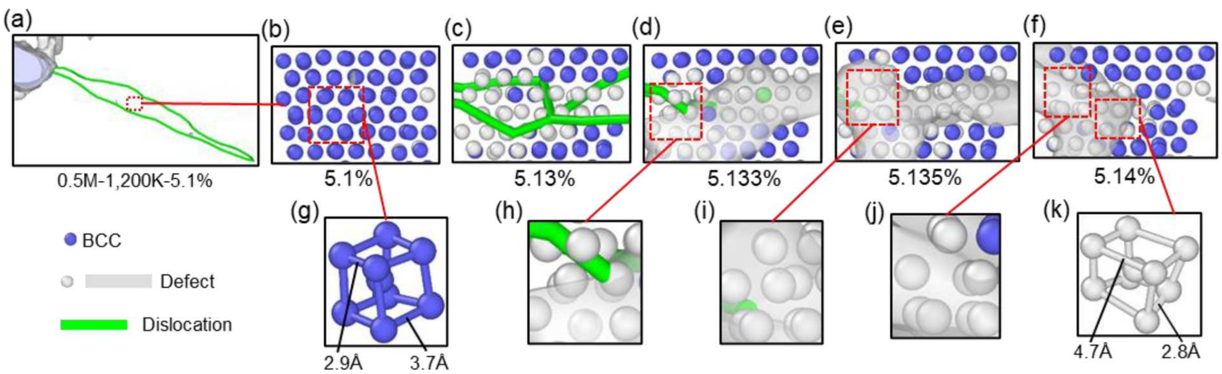

Fig. 10. Dislocation structures, phase structures, and lattice distortions of the MoTaTiWZr RHEA at different strains during tension at 1,200 K. (a) Dislocation structures of the 0.5M-1200 K sample at a 5.1 % strain. Local dislocations and phase (BCC and defect) structures of the 0.5M-1200 K sample at different strains: (b) 5.1 % strain, (c) 5.13 % strain, (d) 5.133 % strain, (e) 5.135 % strain, and (f) 5.14 % strain, as indicated in (a). (g) Normal and (k) severe lattice distortions in the 0.5M-1200 K sample, as indicated in (b) and (f). (h-j) Disordered structures in the 0.5M-1200 K sample, as indicated in (d-f).

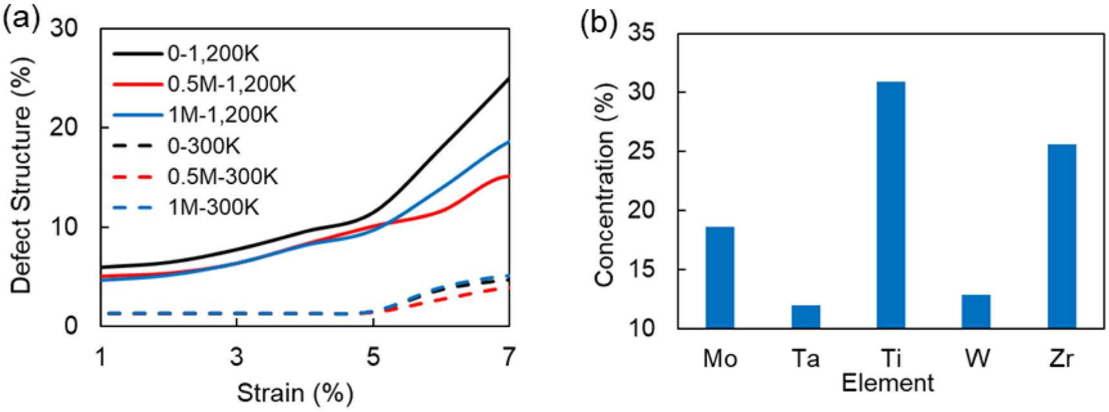

Fig. 11. Ratio of defect structures as a function of the strain and elemental concentrations in the defect structures of the MoTaTiWZr RHEA. (a) Ratio of defect structures as a function of the strain during tension at 300 K and 1,200 K. (b) Elemental concentrations in the defect structures of the 0.5M-1200 K sample under 6 % strain.

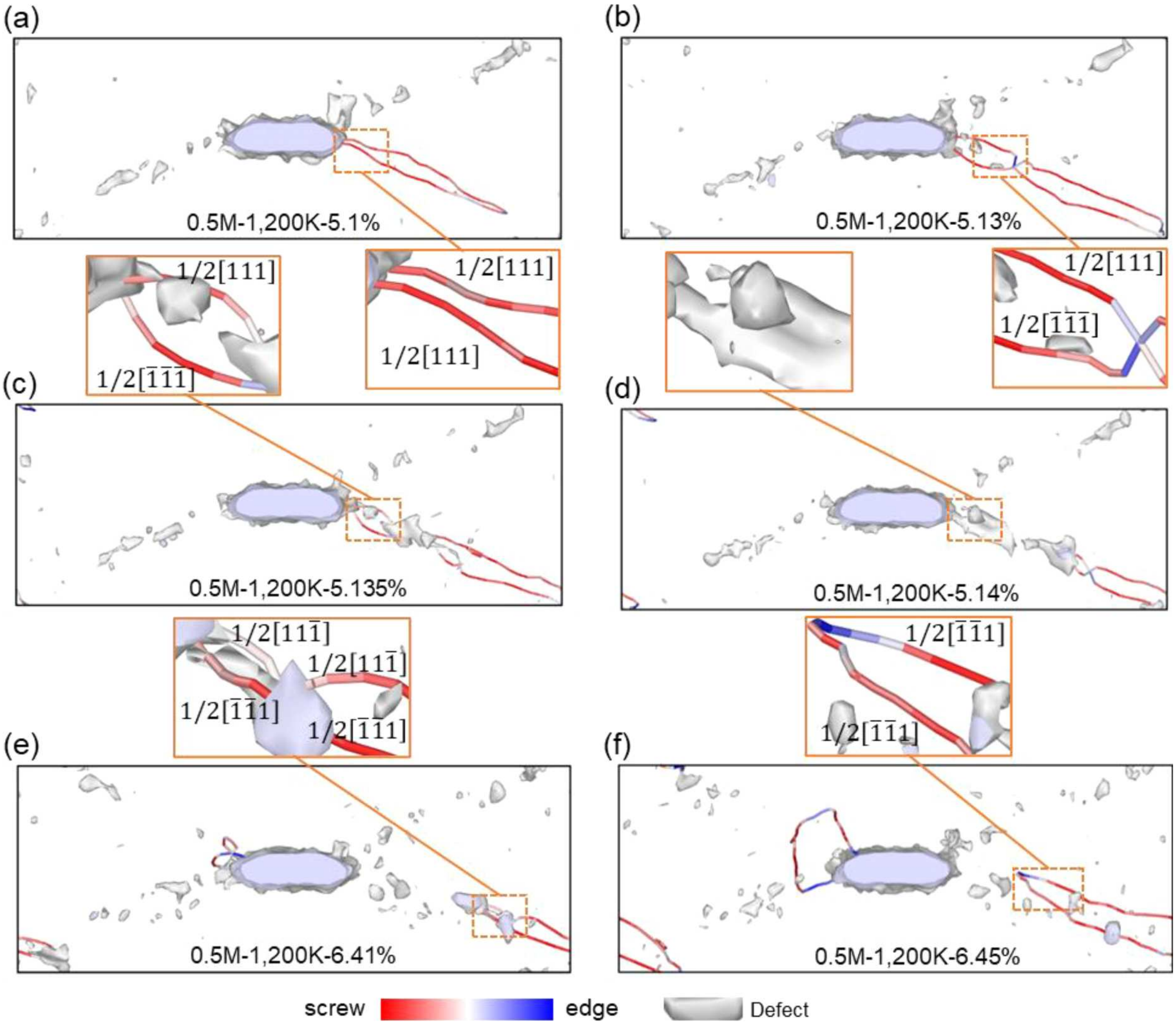

Fig. 12. Dislocation breakup, absorption, and annihilation in the MoTaTiWZr RHEA at 1,200 K. Dislocation structures and characteristics in the 0.5M-1200 K sample at different strains: (a) 5.1 % strain, (b) 5.13 % strain, (c) 5.135 % strain, (d) 5.14 % strain, (e) 6.41 % strain, and (f) 6.45 % strain. The dislocations are screw-character dominated with edge and mixed characters at the breakup and tip positions.

provides useful guidelines for the rational design of RHEAs with high-performance mechanical properties for structural applications.

CRediT authorship contribution statement

Shuai Chen: Investigation, Conceptualization, Methodology, Software, Data curation, Formal analysis, Validation, Visualization, Writing – original draft, Writing – review & editing. **Zachary H. Aitken:** Software, Formal analysis, Writing – review & editing. **Subrahmanyam Pattamatta:** Methodology, Software, Data curation. **Zhaoxuan Wu:** Methodology, Software, Formal analysis. **Zhi Gen Yu:** Resources, Software, Validation, Formal analysis. **David J. Srolovitz:** Formal analysis, Writing – review & editing, Funding acquisition, Supervision. **Peter K. Liaw:** Investigation, Formal analysis, Writing – review & editing, Funding acquisition. **Yong-Wei Zhang:** Conceptualization, Formal analysis, Writing – review & editing, Funding acquisition, Project administration, Supervision.

Declaration of Competing Interest

The authors declare that they have no known competing financial interests or personal relationships that could have appeared to influence the work reported in this paper.

Data availability

Data will be made available on request.

Acknowledgments

The contributions of S. C. in this paper were sponsored by Shanghai Pujiang Program (Grant No. 22PJ1403700) and National Natural Science Foundation of China (Grant No. 52301017). S. C., Z. H. A., Z. G. Y., and YW. Z. gratefully acknowledge the financial support from the Agency for Science, Technology and Research (A*STAR) under grant AMDM A1898b0043, and the use of computing resources at the A*STAR Computational Resource Centre and National Supercomputer Centre, Singapore. This work is also supported by Shanghai Technical Service Center of Science and Engineering Computing, Shanghai University. P. K. L. gratefully acknowledges the support of (1) the National Science Foundation (DMR-1611180, 1809640, and 2226508) with program directors, Drs. J. Madison, J. Yang, G. Shiflet, and D. Farkas and (2) the US Army Research Office (W911NF-13-1-0438 and W911NF-19-2-0049) with program managers, Drs. M. P. Bakas, S. N. Mathaudhu, and D. M. Stepp. The contributions of D. J. S. and S. P. in this paper were fully supported by a grant from the Research Grants Council of the Hong Kong Special Administrative Region, China (Project No. 11211019).

References

[1] Cantor B, Chang ITH, Knight P, Vincent AJB. Microstructural development in equiatomic multicomponent alloys. Mater Sci Eng, A 2004;375:213–8.
[2] Yeh JW, et al. Nanostructured high-entropy alloys with multiple principal elements: novel alloy design concepts and outcomes. Adv Eng Mater 2004;6: 299–303.
[3] George EP, Raabe D, Ritchie RO. H.igh-entropy alloys. Nat Rev Mater 2019;4: 515–34.
[4] Yang T, et al. Ultrahigh-strength and ductile superlattice alloys with nanoscale disordered interfaces. Science 2020;369:427–32.
[5] Cantor B. Multicomponent high-entropy Cantor alloys. Prog Mater Sci 2021;120: 100754.
[6] Lee C, et al. Temperature dependence of elastic and plastic deformation behavior of a refractory high-entropy alloy. Sci Adv 2020;6:eaaz4748.
[7] Lee C, et al. Strength can be controlled by edge dislocations in refractory high-entropy alloys. Nat Commun 2021;12:5474.
[8] Li T, et al. CALPHAD-aided design for superior thermal stability and mechanical behavior in a TiZrHfNb refractory high-entropy alloy. Acta Mater 2023;246: 118728.
[9] Atwani OE, et al. A quinary WTaCrVHf nanocrystalline refractory high-entropy alloy withholding extreme irradiation environments. Nat Commun 2023;14:2516.
[10] Liu CJ, et al. Tensile creep behavior of HfNbTaTiZr refractory high entropy alloy at elevated temperatures. Acta Mater 2022;237:118188.
[11] Cheng Z, Wang S, Wu G, Gao J, Yang X, Wu H. Tribological properties of high-entropy alloys: a review. Int J Miner Metall Mater 2022;29:389–403.
[12] Ye W, et al. Microstructure and tribological properties of *in-situ* carbide/ CoCrFeNiMn high entropy alloy composites synthesized by flake powder metallurgy. Tribol Int 2023;181:108295.
[13] Chen B, Li S, Zong H, Ding X, Sun J, Ma E. Unusual activated processes controlling dislocation motion in body-centered-cubic high-entropy alloys. Proc Natl Acad Sci U S A 2020;117:16199–206.
[14] Varvenne C, Luque A, Curtin WA. T.heory of strengthening in FCC high entropy alloys. Acta Mater 2016;118:164–76.
[15] Maresca F, Curtin WA. M.echanistic origin of high strength in refractory BCC high entropy alloys up to 1900K. Acta Mater 2020;182:235–49.
[16] Yin B, Maresca F, Curtin WA. V.anadium is an optimal element for strengthening in both fcc and bcc high-entropy alloys. Acta Mater 2020;188:486–91.
[17] Wei S, et al. Natural-mixing guided design of refractory high-entropy alloys with as-cast tensile ductility. Nat Mater 2020;19:1175–81.
[18] Wang Z, et al. Solving oxygen embrittlement of refractory high-entropy alloy via grain boundary engineering. Mater Today 2022;54:83–9.
[19] Gou S, et al. Additive manufacturing of ductile refractory high-entropy alloys via phase engineering. Acta Mater 2023;248:118781.
[20] Li T, et al. Ultra-strong tungsten refractory high-entropy alloy via stepwise controllable coherent nanoprecipitations. Nat Commun 2023;14:3006.
[21] Rice JR. D.islocation nucleation from a crack tip: an analysis based on the Peierls concept. J Mech Phys Solid 1992;40:239–71.
[22] Hu YJ, Sundar A, Ogata S, Qi L. Screening of generalized stacking fault energies, surface energies and intrinsic ductile potency of refractory multicomponent alloys. Acta Mater 2021;210:116800.
[23] Tong Y, Zhao S, Bei H, Egami T, Zhang Y, Zhang F. Severe local lattice distortion in Zr- and/or Hf-containing refractory multi-principal element alloys. Acta Mater 2020;183:172–81.
[24] Ding Q, et al. Tuning element distribution, structure and properties by composition in high-entropy alloys. Nature 2019;574:223–7.
[25] Hsiao HW, et al. Data-driven electron-diffraction approach reveals local short-range ordering in CrCoNi with ordering effects. Nat Commun 2022;13:6651.
[26] Zhang R, et al. Short-range order and its impact on the CrCoNi medium-entropy alloy. Nature 2020;581:283–7.
[27] Chen X, et al. Direct observation of chemical short-range order in a medium-entropy alloy. Nature 2021;592:712–6.
[28] Lee C, et al. Lattice distortion in a strong and ductile refractory high-entropy alloy. Acta Mater 2018;160:158–72.
[29] Ma E, Wu X. Tailoring heterogeneities in high-entropy alloys to promote strength-ductility synergy. Nat Commun 2019;10:5623.
[30] Chen S, et al. Simultaneously enhancing the ultimate strength and ductility of high-entropy alloys via short-range ordering. Nat Commun 2021;12:4953.
[31] Ren Y, et al. Friction-induced rapid amorphization in a wear-resistant (CoCrNi)$_{88}$Mo$_{12}$ dual-phase medium-entropy alloy at cryogenic temperature. Compos B Eng 2023;263:110833.
[32] Zunger A, Wei SH, Ferreira LG, Bernard JE. S.pecial quasirandom structures. Phys Rev Lett 1990;65:353–6.
[33] Jiang C, Uberuaga BP. E.fficient ab initio modeling of random multicomponent alloys. Phys Rev Lett 2016;116:105501.
[34] Sorkin V, Chen S, Tan TL, Yu ZG, Man M, Zhang YW. First-principles-based high-throughput computation for high entropy alloys with short range order. J Alloy Compd 2021;882:160776.
[35] Alvarado AM, et al. Predicting short-range order evolution in WTaCrVHf refractory high-entropy alloys. Scr Mater 2023;233:115506.
[36] Li XG, Chen C, Zheng H, Zuo Y, Ong SP. Complex strengthening mechanisms in the NbMoTaW multiprincipal element alloy. NPJ Comput Mater 2020;6:70.
[37] Xie H, Ma Z, Zhang W, Zhao H, Ren L. Phase transition in shock compressed high-entropy alloy FeNiCrCoCu. Int J Mech Sci 2023;238:107855.
[38] Gao T, et al. Molecular dynamics simulations of tensile response for FeNiCrCoCu high-entropy alloy with voids. Int J Mech Sci 2023;237:107800.
[39] Zhou Q, et al. Design and characterization of metallic glass/graphene multilayer with excellent nanowear properties. Friction 2022;10:1913–26.
[40] Chen S, et al. Chemical-affinity disparity and exclusivity drive atomic segregation, short-range ordering, and cluster formation in high-entropy alloys. Acta Mater 2021;206:116638.
[41] He T, Qi Y, Ji Y, Feng M. Grain boundary segregation-induced strengthening-weakening transition and its ideal maximum strength in nanopolycrystalline FeNiCrCoCu high-entropy alloys. Int J Mech Sci 2023;238:107828.
[42] Li W, Chen S, Aitken Z, Zhang YW. Shock-induced deformation and spallation in CoCrFeMnNi high-entropy alloys at high strain-rates. Int J Plast 2023;168:103691.
[43] Yin S, et al. Atomistic simulations of dislocation mobility in refractory high-entropy alloys and the effect of chemical short-range order. Nat Commun 2021;12:4873.
[44] Wang X, Maresca F, Cao P. The hierarchical energy landscape of screw dislocation motion in refractory high-entropy alloys. Acta Mater 2022;234:118022.
[45] Chen S, et al. Short-range ordering alters the dislocation nucleation and propagation in refractory high-entropy alloys. Mater Today 2023;65:14–25.
[46] Cowley JM. Xray measurement of order in single crystals of Cu$_3$Au. J Appl Phys 1950;21:24–30.
[47] Zhou XW, et al. Misfit-energy-increasing dislocations in vapor-deposited CoFe/ NiFe multilayers. Phys Rev B 2004;69:144113.

[48] Plimpton S. Fast parallel algorithms for short-range molecular dynamics. J Comput Phys 1995;117:1–19.

[49] Singh P, et al. Design of high-strength refractory complex solid-solution alloys. NPJ Comput Mater 2018;4:16.

[50] Sharma A, et al. Pseudoelastic deformation in Mo-based refractory multi-principal element alloys. Acta Mater 2021;220:117299.

[51] Zhou XY, Zhu JH, Wu Y, Yang XS, Lookman T, Wu HH. Machine learning assisted design of FeCoNiCrMn high-entropy alloys with ultra-low hydrogen diffusion coefficients. Acta Mater 2022;224:117535.

[52] Xu S, Hwang E, Jian WR, Su Y, Beyerlein IJ. A.tomistic calculations of the generalized stacking fault energies in two refractory multi-principal element alloys. Intermetallics 2020;124:106844.

[53] Nitzan A. Chemical dynamics in condensed phases: relaxation, transfer and reactions in condensed molecular systems. Oxford University Press; 2006.

[54] Metropolis N, Rosenbluth AW, Rosenbluth MN, Teller AH, Teller E. Equation of state calculations by fast computing machines. J Chem Phys 1953;21:1087–92.

[55] Stukowski A, Bulatov VV, Arsenlis A. Automated identification and indexing of dislocations in crystal interfaces. Model Simul Mater Sci Eng 2012;20:085007.

[56] Stukowski A. Visualization and analysis of atomistic simulation data with OVITO-the open visualization tool. Model Simul Mater Sci Eng 2009;18:15012.

[57] Mei ZG, Shang SL, Wang Y, Liu ZK. Density-functional study of the thermodynamic properties and the pressure-temperature phase diagram of Ti. Phys Rev B 2009;80:104116.

[58] Lei Z, et al. Enhanced strength and ductility in a high-entropy alloy via ordered oxygen complexes. Nature 2018;563:546–50.

[59] Zhang B, Ding J, Ma E. Chemical short-range order in body centered-cubic TiZrHfNb high-entropy alloys. Appl Phys Lett 2021;119:201908.

[60] Xun K, Zhang B, Wang Q, Zhang Z, Ding J, Ma E. Local chemical inhomogeneities in TiZrNb-based refractory high-entropy alloys. J Mater Sci Technol 2023;135:221–30.

[61] Barzilai S, Toher C, Curtarolo S, Levy O. Evaluation of the tantalum-titanium phase diagram from ab-initio calculations. Acta Mater 2016;120:255–63.

[62] Chinnappan R, Panigrahi BK, Walle AVD. First-principles study of phase equilibrium in Ti–V, Ti–Nb, and Ti–Ta alloys. Calphad 2016;54:125.

[63] Shim JH, Oh CS, Lee DN. A. thermodynamic evaluation of the Ti-Mo-C system. Metall Mater Trans B 1996;27B:955.

[64] Ångqvist M, Rahm JM, Gharaee L, Erhart P. Structurally driven asymmetric miscibility in the phase diagram of W-Ti. Phys Rev Mater 2019;3:073605.

[65] Sobieraj D, et al. Chemical short-range order in derivative Cr–Ta–Ti–V–W high entropy alloys from the first-principles thermodynamic study. Phys Chem Chem Phys 2020;22:23929.

[66] Li H, et al. Fatigue behavior, microstructural evolution, and fatigue life model based on dislocation annihilation of an Fe-Ni-Cr alloy at 700°C. Int J Plast 2019;118:105–29.

[67] Liu L, et al. Nanoprecipitate-strengthened high-entropy alloys. Adv Sci 2021;8:2100870.